

Lateral Variations and Azimuthal Isotropy of P_n Velocities Beneath Basin and Range Province

LIAN-SHE ZHAO¹

Seismological Laboratory, California Institute of Technology, Pasadena

Travel time tomography was used to obtain the lateral variations in P_n velocities and P_n velocity azimuthal anisotropy beneath the Basin and Range Province. We used 1226 P_n arrivals from 184 earthquakes recorded by 113 stations. The tomographic image shows the lateral variation in P_n velocity from 7.9 km s^{-1} in the northern Province to 7.6 km s^{-1} in the southern Province. Azimuthal variations in P_n velocities are less than one percent as determined from the travel time residuals after taking out the contribution of the lateral velocity variations of the P_n tomography. Although the standard errors of the azimuthal variations are $\sim 2\%$, there is no reason to believe the existence of the P_n azimuthal anisotropy in the uppermost mantle beneath the Basin and Range Province. Beghoul and Barazangi's (1990) suggestion of more than 3% azimuthal anisotropy is the result of the lateral heterogeneity and mantle velocity gradient. Before tomographic inversion, we refined the P_n travel times by considering the lateral variations in the crustal thickness and velocities in the region based on the numerical experiment and theoretical development given in this paper. These refinements are crucial in obtaining an accurate velocity image. The average velocity is $7.72 \pm 0.16 \text{ km s}^{-1}$, and an average vertical mantle velocity gradient is $8.0 \times 10^{-4} \text{ s}^{-1}$. The resolution for P_n velocity image is generally within 2° to 5° .

INTRODUCTION

Anisotropy, a characteristic of many mantle minerals, is important to seismology since it is responsible for the large variations in seismic velocities. Some researchers have suggested seismic velocity variations due to anisotropy are potentially much greater than those due to other effects such as composition and temperature. Thus it is necessary to understand seismic anisotropy well before one attempts to infer chemical, mineralogical, and temperature variations from seismic data [e.g., Anderson, 1989]. However, some evidence of the existence of seismic anisotropy can be interpreted as the lateral heterogeneity of the structure, since there is often a direct trade-off between anisotropy and heterogeneity. In order to circumvent this problem, we present a method of identifying P_n velocity azimuthal anisotropy in the presence of the lateral heterogeneity of the crustal and upper mantle.

An anisotropic upper mantle would be expected if it is olivine-rich [e.g., Anderson, 1989, p. 306; Duffy and Anderson, 1989]. Crystal alignment may be caused by the motions in the mantle associated with mantle convection, internal deformation of the lithosphere, the preferred local stress field orientation, or recrystallization. Thus attempts at finding evidence of seismic anisotropy are largely focused on tectonically active regions in the world. Because of limited data and complexity of the Earth, especially in tectonically active regions, it is difficult to identify anisotropy unambiguously in the presence of structural heterogeneity. In order to minimize the contribution of heterogeneity, researchers have turned to shear wave splitting to try to find anisotropy, [e.g., Savage et al., 1990; Silver and Chan, 1988, 1991; Xie, 1992]. Numerical experiments show that coupled

mode waveform anomalies of surface waves in the frequency range of 0-20 mHz can be diagnostic of upper mantle azimuthal anisotropy [Park and Yu, 1992; Tanimoto and Anderson, 1985; Yu and Park, 1993].

P_n travel times have been used to find evidence for the existence of azimuthal anisotropy [e.g., Bamford et al., 1979; Beghoul and Barazangi, 1990; Hess, 1964; Rait et al., 1971; Vetter and Minster, 1981]. For the Basin and Range province, Beghoul and Barazangi [1990] suggested a 3.2% azimuthal anisotropy in P_n velocity. In this study, we rigorously examine P_n velocities beneath the Basin and Range province. We used all possible International Seismological Centre (ISC) P_n travel times from 1964 to 1990. We account for the three-dimensional local crustal and mantle velocity structure (including the topography of the surface and the Moho) to refine the apparent P_n velocities before inversion, employing the numerical method discussed in detail later. After tomographic inversion, we allocated the non diminished P_n travel time residuals back to the vertical travel times of the source and receiver. This process is actually the source relocation and local velocity structure refinement. After this process, we obtain a new data set of apparent P_n velocities. We then invert the new data set and allocate the non diminished residuals after inversion again until the allocation is so small that the results of the last two iterations are almost the same. In this study we used four iterations. After the whole process is done, we assume that the non diminished P_n travel time residuals are mainly due to the azimuthal velocity dependence, since the contribution of lateral variation of the P_n velocities are taken out by the tomographic inversion. Thus we can find out if P_n velocity residuals calculated from travel time residuals depend on azimuth.

¹Now at Institute for Geophysics, University of Texas at Austin.

DATA

Using the ISC database, we collected 1226 P_n travel times from 184 earthquakes ($M_L > 2.9$) that occurred in or around the Basin and Range province from 1964 to 1990, recorded at 113 stations. The ray paths are shown in Figure

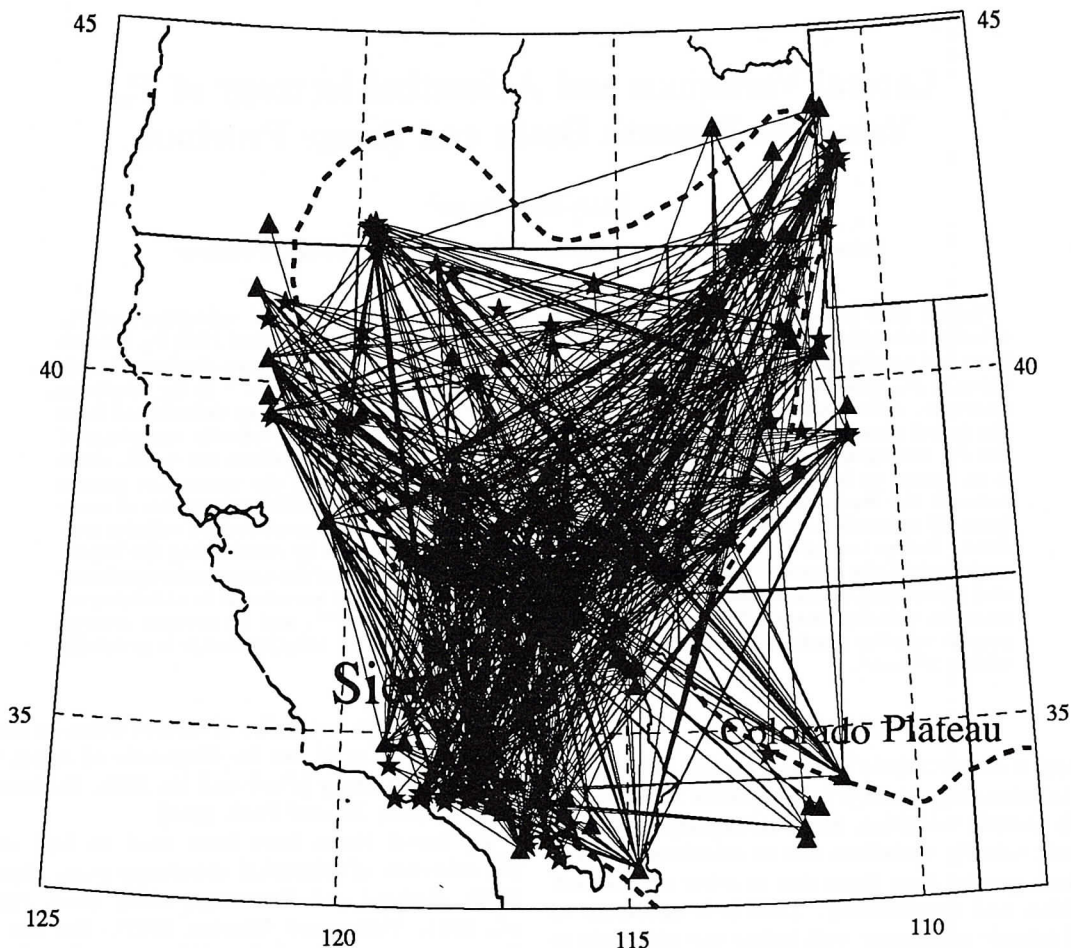


Fig. 1. Ray paths. Triangles represent stations and stars represent earthquakes. Heavy dashed lines depict the boundaries of the Basin and Range province. State boundaries are also included.

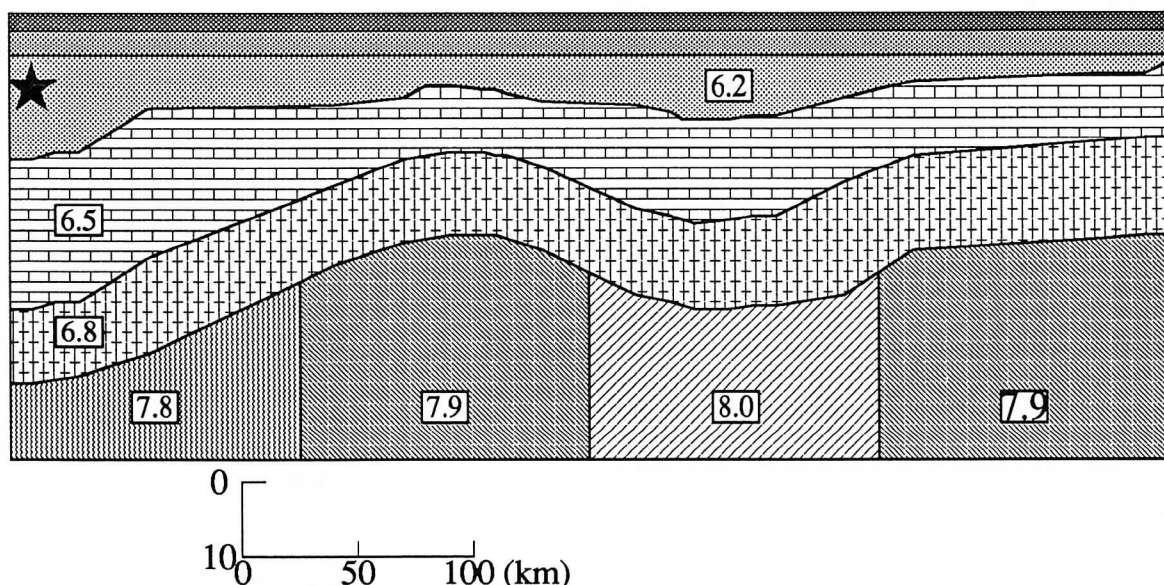


Fig. 2. Two-dimensional model used to generate finite difference synthetic seismograms. The velocities for blocks are given in the boxes. The velocity is 5.2 km s^{-1} for the layer at the top, for the layer beneath it, the velocity is 6.0 km s^{-1} . The star is the source.

1. We selected paths for which the apparent P_n velocity is between 7.0 - 8.5 km s⁻¹, after correcting the average crustal thickness of 35 km [Braile et al., 1989]. The distance range is 2°- 11°.

METHOD AND PROCEDURE

We begin with the observed P_n travel times t_{obs} , which can be written as

$$t_{obs} = \alpha + \beta + \gamma + \int_s^r Sdl, \quad (1)$$

where α is the vertical travel time from source to Moho, β is the vertical travel time from Moho to receiver, and γ is the contribution of the vertical velocity gradient of the mantle. The horizontal travel time, $\int_s^r Sdl$ is from source s to receiver r where S is local slowness. In the following, we give a detailed description how to estimate α , β , and γ .

Two Dimensional Crustal Velocity Structure

In a crustal structure with weak heterogeneity, α and β can be written approximately as

$$\alpha = \sum_{j=1}^{j=n_s} \eta_j H_j, \quad \beta = \sum_{i=1}^{i=n_r} \eta_i H_i, \quad (2)$$

where n_s and n_r are the numbers of layers beneath the source and the receiver to the local Moho, respectively. H_j is the layer thickness beneath the source, while H_i is the layer thickness beneath the receiver, $\eta_i = (1/v_i^2 - p^2)^{1/2}$ layer thickness beneath the receiver, where v_i is velocity, and p is the ray parameter. The vertical travel time α is calculated from the velocity structure close to the source, and the vertical travel time β is calculated from the structure close to the receiver (the topography of the surface can be easily included).

We can show the validity of (2) by comparing with finite difference synthetic seismograms [Vidale et al., 1985]. Figure 2 gives a two-dimensional model, for which the crustal thickness varies from 50 to 30 km. Figure 3 gives the finite difference synthetics of the model (solid lines, which are truncated seismograms), predictions of (2) (dagger symbols), and picks (with 0.1-s error bar) from the synthetics (solid circles). The maximum difference between picked and calculated travel times is 0.3 s, which contrast greatly with the more than 1-s difference in the reduced travel times for all traces. Assuming the model at the source end is the model for the whole path, we have a reduced travel time of 7.9 s. In contrast, the reduced travel time is only 4.6 s if using the model at 200 km from the source as the model for the whole path. Thus (1) is a good approximation for the head travel times in two-dimensional velocity structures. If the crustal velocity structure does not change very rapidly in a few tens of kilometers (order of the crustal thickness) in horizontal direction, the error of the predictions of (2) is very small (see the 210-270 km and 360-470 km ranges of Figures 2 and 3).

The model used to estimate α is the model at 50 km from the source, roughly the distance from the source to Moho. For β , the model used is at 40 km to the receiver. If the velocity structure is roughly the same in a few tens of kilometers in the horizontal direction, which is not true for the model given in Figure 2, we can use the velocity structure below the source and receiver to estimate α and β of (2).

The absolute travel times of finite difference synthetic seismograms are refined by comparing the finite difference results of an averaged one-dimensional model of the two-dimensional model used (Figure 2). For one-dimensional models, the head wave travel times can be calculated analytically. The highest-frequency end of the synthetics is 1 Hz. In the complex structures the picked P_n time may not be the minimum travel time for the model, because the energy of the phase may be too small to be noticed.

The good approximation of (1) and (2) can be understood theoretically. The head waves travel almost horizontally in the mantle, so that the horizontal travel time would be approximately the integral in (1). The head wave travel time would be the minimum travel time, so the ray has the critical angle of incidence to the local Moho at the source and leaves the local Moho at the critical angle to go

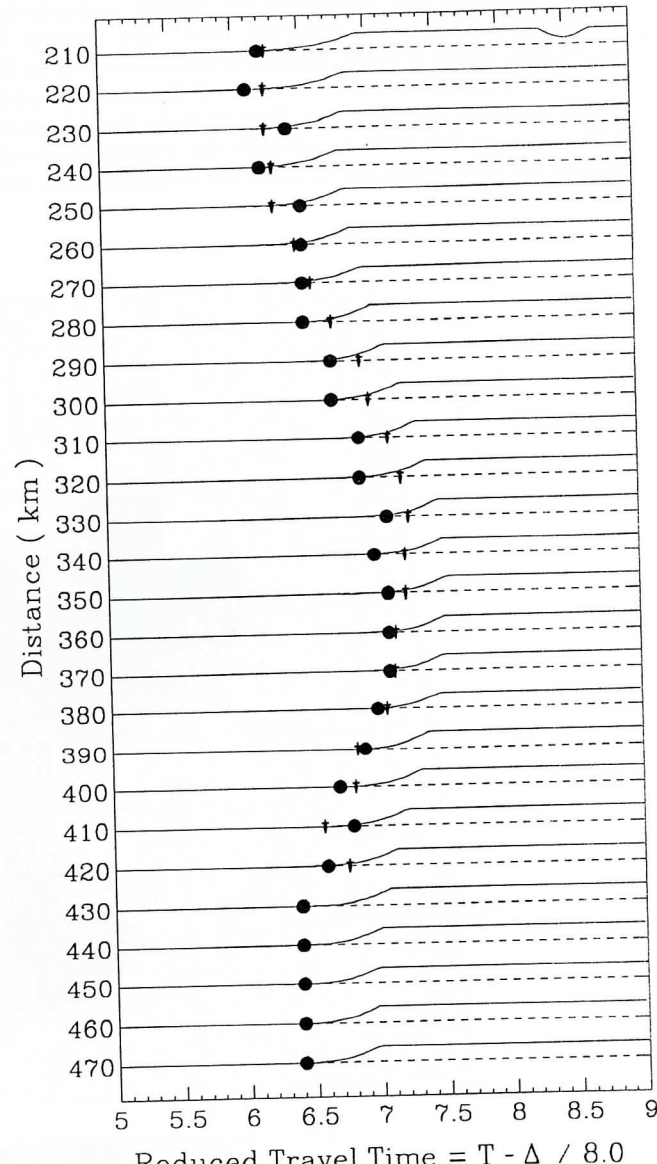


Fig. 3. Comparison of the theoretical calculations using (1) and (2) with the numerical calculation using finite difference synthetic seismogram method. The solid lines are truncated synthetic seismograms, and the solid circles are the travel time picks from the truncated seismograms, and the dagger symbols are the theoretical calculations. The model used is given in Figure 2.

to the receiver. Equation (1) is a good approximation as long as the structure is sufficiently close to one-dimensional, since the ray parameter p is no longer a constant in two-dimensional velocity structures.

A Constant Velocity Gradient Mantle

If a mantle has a constant velocity gradient, then the travel times of head waves are not a linear function of distance. If we use the form

$$v = v_0(1 + cz) \quad (3)$$

to represent the velocities in the mantle, where z is the depth from Moho (downward is positive), c is a constant whose product with v_0 gives the mantle velocity gradient for a flat Earth. For a spherical Earth, the velocity gradient is $(c - 1.58 \times 10^{-4})v_0$ when the units for c and v_0 are given in per kilometers and kilometers per second, respectively [Helmberger, 1973]. The observed head wave velocity is $v_{obs} = X/t$, where X is the horizontal distance traveling in the mantle, and t is the minimum travel time of the model at this distance (we used v_{obs} here because its definition is the same as that used to estimate the average observed velocity for head waves and to show the difference from the

conventionally used head wave velocity of v_0). The observed head wave velocity v_{obs} can be written as

$$v_{obs} \approx v_0 + \frac{c^2 v_0}{24} X^2, \quad (4)$$

when $c \ll 1$, which usually holds for the real Earth. Equation (4) is valid when $X < X_m = ((1 + cH_m)^2 - 1)^{1/2}/c$, where H_m is the maximum depth that (3) holds. When $X > X_m$, we have

$$v_{obs} \approx v_0 + v_0 c H_m (1 - \frac{2X_m}{3X}) \quad (5)$$

The derivations of (4) and (5) are given in the appendix.

From (4) and (5), γ in (1) can be written as

$$\gamma \approx -\frac{X}{v_0} \frac{\delta v}{v_0}, \quad (6)$$

where δv is the second term in (4) or (5).

Inversion Method

Once α and β are calculated from (2) and the local velocity structure is removed from t_{obs} in (1), we have

$$v_{obs} = D/(t_{obs} - \alpha' - \beta') \quad X = D - A - B, \quad (7)$$

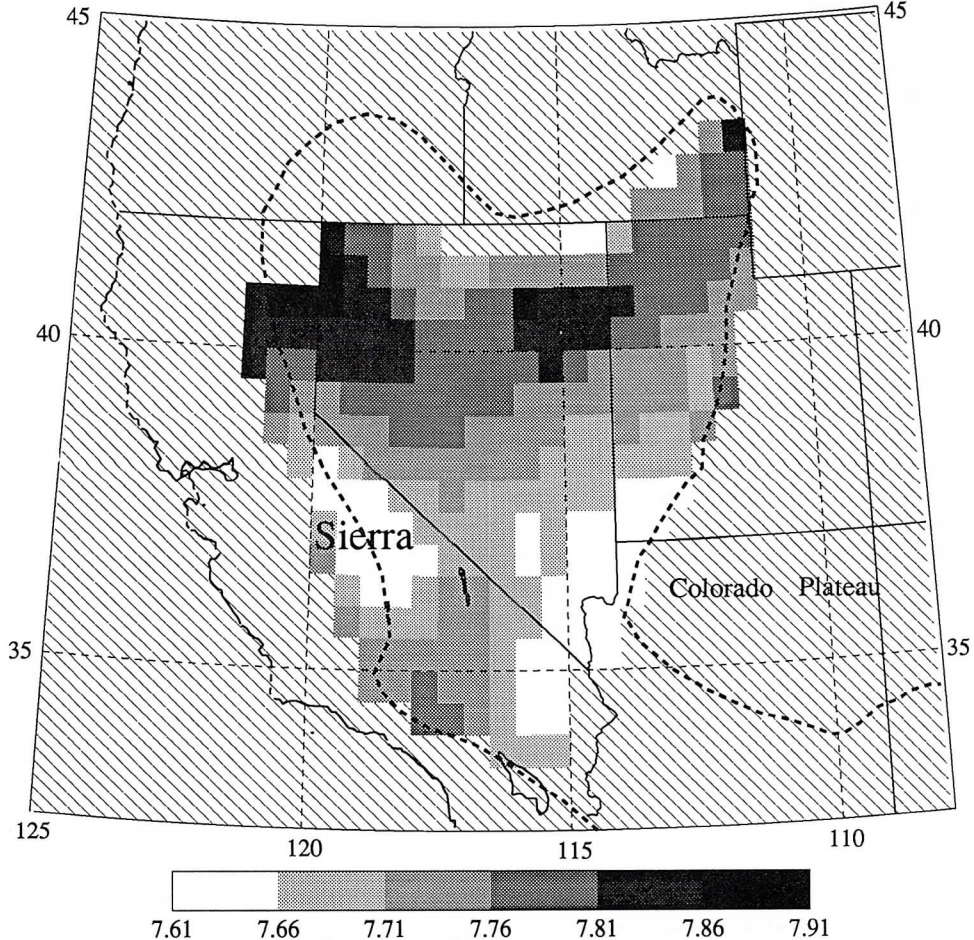


Fig. 4. P_n velocity image for the Basin and Range province. Heavy dashed lines depict the boundaries of the Basin and Range province. The diagonally ruled area indicates an area with insufficient resolution.

where D is the horizontal source-receiver distance, the primed quantities are estimated ones from available information. A and B , the horizontal travel distances of the P_n ray in the crust beneath the source and receiver, can be estimated from local crustal model. For every path, once v_{obs} and X are determined, we can calculate c from Eqs. (4) and (5) using the least squares method, and then γ from (6).

For each of (i, j) , source i to receiver j , we have:

$$\left(\int_s^r Sdl \right)_{ij} = \sum_k \Delta_{ijk} s_k = (t_{obs})_{ij} - \alpha'_i - \beta'_j - \gamma'_{ij} - RES_{ij}, \quad (8)$$

where Δ_{ijk} is the length of the line segment over which the (i, j) th path overlaps the k th grid, s_k is the slowness in the k th grid, and the travel time residual for (i, j) path is

$$\begin{aligned} RES_{ij} &= \delta\alpha_i + \delta\beta_j + \delta\gamma_{ij} \\ &= (\alpha_i - \alpha'_i) + (\beta_j - \beta'_j) + (\gamma_{ij} - \gamma'_{ij}). \end{aligned}$$

Then (8) can be rewritten as

$$\sum_k \Delta_{ijk} s_k + RES_{ij} = (t_{obs})_{ij} - \alpha'_i - \beta'_j - \gamma'_{ij}. \quad (9)$$

The right-hand side of (9) is known. This equation forms a standard linear inverse problem for unknown s_k . We used a back projection, or SIRT algorithm [e.g. Humphreys and Clayton, 1998; Xie and Mitchell, 1990] to solve for s_k . In particular, we use the nine-grid smoothing operation [Suet-sugu and Nakanishi, 1985; Xie and Mitchell, 1990] between iterations. This operation is used to overcome insufficient spatial data coverage, at a slight cost to resolution.

Method to Refine α and β

In the back projection calculation, s_k values are updated during the iterations to reduce the misfit of left-hand and right-hand side of (9). When the misfit stops decreasing, we end up with the final slowness model (values of s_k) and some non-diminished RES_{ij} values. To the first-order approximation we assume that RES_{ij} are dominantly caused by imprecise estimates on α_i and β_j ; we then have

$$RES_{ij} \approx \delta\alpha_i + \delta\beta_j. \quad (10)$$

Non zero $\delta\alpha$ are primarily due to the mislocation of the source (location, depth, and origin time), and the erroneous crustal structure used before the inversion, and non zero $\delta\beta$ is purely from erroneous crustal structure. Equation (10) also forms a linear inversion problem, for which we used the least squares method to allocate RES_{ij} back to α_i and β_j . This means that the sources are relocated and the local crustal models for the source and receiver regions have been improved in the new slowness model.

After new α_i and β_j are determined, we implement the back projection calculation again to update s_k model, then update α and β again, until the maximum of the allocations $\delta\alpha$ and $\delta\beta$ of α and β reaches some small limit.

Method of Estimating Azimuthal Anisotropy

Since the velocity image (s_k model) is an average in all directions, it is reasonable to assume that the non zero travel time residuals RES_{ij} result mainly from the possible azimuthal anisotropy, after all inversion process in the earlier sections is done. We define the velocity residual as

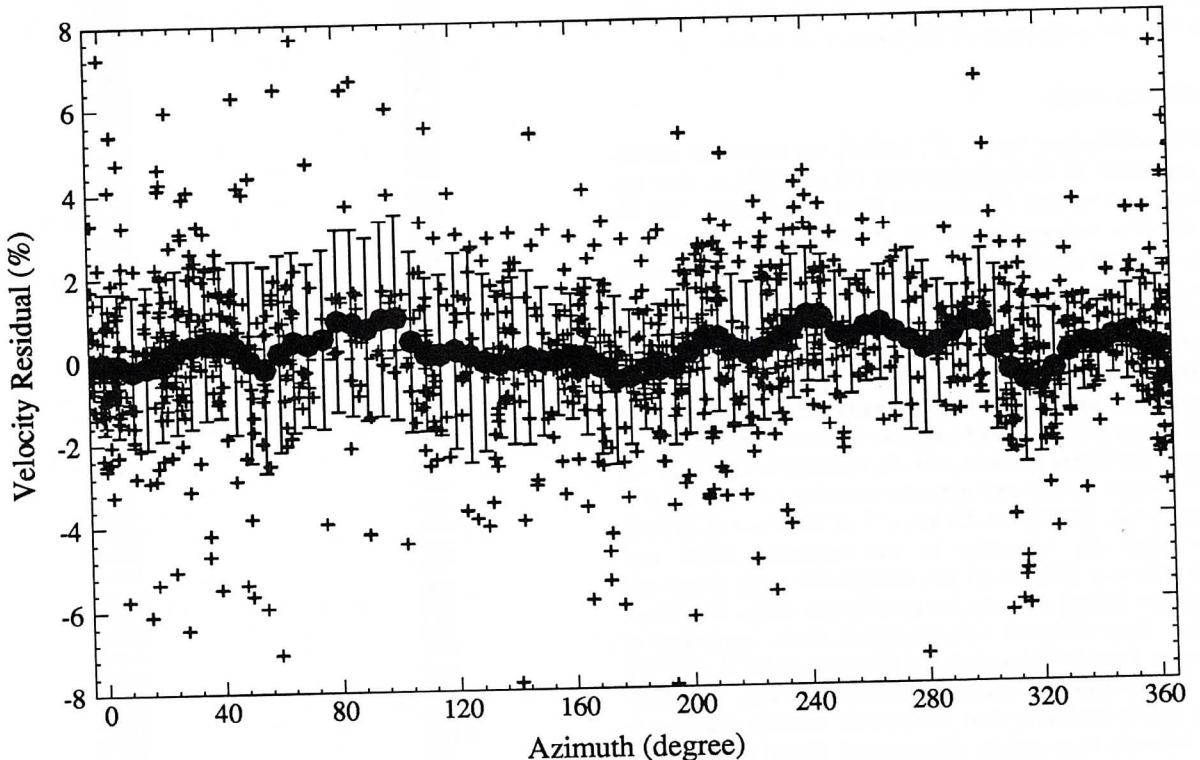


Fig. 5. Velocity residuals ($\delta v/v$ in percent) calculated by using (11) (plus signs), and average velocity residuals (Equation (12)) in the 20° interval (solid circles) with error bars (square root of (13)), versus the azimuths of the paths.

$$\frac{\delta v}{v} = \frac{v_{obs} - v_{syn}}{v_{syn}} = \frac{RES}{t_{obs} - \alpha - \beta - \gamma}. \quad (11)$$

For one particular azimuth θ , we use average

$$(\frac{\delta v}{v})_{av} = \frac{\sum_{\theta=10}^{\theta+10} (6 - \frac{|\theta_i - \theta|}{2})(\frac{\delta v}{v})_i}{\sum_{\theta=10}^{\theta+10} (6 - \frac{|\theta_i - \theta|}{2})} \quad (12)$$

as the velocity residuals at this azimuth, where i is the path within the 20° interval. Also, we use the square root of

$$\frac{\sum_{\theta=10}^{\theta+10} (6 - \frac{|\theta_i - \theta|}{2})((\frac{\delta v}{v})_i - (\frac{\delta v}{v})_{av})^2}{\sum_{\theta=10}^{\theta+10} (6 - \frac{|\theta_i - \theta|}{2})} \quad (13)$$

as the standard deviation of this velocity residual.

RESULTS

We used the resulting models of seismic sounding studies [Braile et al., 1989] as local models to estimate α and β and obtained α' and β' values for the source and the receiver delays, calculated from (2). In this estimation we assumed that the velocity structure does not vary rapidly. The topography of the surface of the Earth is included.

Mantle Velocity Gradient

Using Burdick and Helmberger's [1978] T7 model, which was proposed for the western United States, we can get an estimate for X_m of 2400 km, much greater than the maximum distance we used in this study. Thus we can use (4) and (7) to estimate c and obtain $c = 2.56 \times 10^{-4} \text{ km}^{-1}$, which is the average for all ray paths, and mantle velocity gradient $2.0 \times 10^{-3} \text{ s}^{-1}$, including the contribution of the Earth's sphericity $1.2 \times 10^{-3} \text{ s}^{-1}$. γ' can be estimated by using (6). At a distance of 1200 km, γ' is -0.6 s.

P_n Velocity Image

After accounting for α' , β' , and γ' , we used four allocation iterations to find solutions for (9) and (10) so that the maximum of $\delta\alpha$ and $\delta\beta$ was less than 0.2 seconds. We divide the area between 29° - 47° N and 107° - 126° W into 1406 blocks of a size of $0.5^\circ \times 0.5^\circ$. Figure 4 gives the final velocity image. The average velocity of this image is $7.72 \pm 0.16 \text{ km s}^{-1}$. (The P_n velocities are given at depth of 30 km.) The velocity image shows a faster velocity in the north and a slower velocity in the south (Figure 4). The slow velocity regions in the uppermost mantle beneath Sierra Madre and the southern end of Nevada appear to be connected.

Along the Sierra Nevada, the P_n velocity is less than 7.7 km s^{-1} , which agrees well with the velocity 7.6 - 7.65 km s^{-1} of Jones et al. [1993], 7.6 - 7.7 km s^{-1} of Hearn et al. [1991].

The slow P_n velocities in the southern Basin and Range province (Figure 4) are compatible with Biasi and Humphreys' [1992] velocity image of depth range 30-60 km. However, they obtained a faster region at the northwest of Southwest Nevada Volcanic Field (roughly at 38° N, 117° W) closer to the Nevada boundary than this study. The reason for this is probably that the mantle velocity gradient is larger beneath that region. Hearn et al. [1991] also found a slow region in the south, albeit a much smaller one, which may be because of the flat Moho assumption used in their study. We will return to this later.

Azimuthal Anisotropy

The analysis of the travel time residuals, after the inversion and allocation procedure is done, is given in Figure 5, in 5° spacing, using (12) and (13). The denominators, $\sum_{\theta=10}^{\theta+10} (6 - \frac{|\theta_i - \theta|}{2})$, in (12) and (13) are given in Table 1. The value of the denominator at one azimuth repre-

TABLE 1. The denominator of (12) and (13),

θ	$\sum_{\theta=10}^{\theta+10} (6 - \frac{ \theta_i - \theta }{2})$	SUM
0		452.0
5		449.2
10		335.2
15		318.9
20		395.4
25		394.4
30		339.9
35		311.8
40		311.6
45		282.7
50		224.5
55		192.3
60		195.6
65		186.6
70		136.4
75		90.6
80		103.9
85		122.0
90		115.2
95		112.3
100		128.2
105		184.1
110		220.2
115		210.6
120		190.2
125		203.8
130		223.1
135		232.2
140		226.4
145		177.9
150		183.5
155		278.9
160		358.4
165		375.8
170		319.0
175		243.6
180		228.7
185		265.9
190		316.1
195		316.4
200		331.4
205		371.8
210		342.9
215		284.7
220		279.0
225		319.2
230		320.4
235		285.8
240		255.6
245		221.0
250		174.5
255		136.2
260		124.3
265		93.0
270		74.2
275		70.5
280		94.7
285		145.5
290		168.8
295		180.3
300		200.7
305		251.3
310		324.3
315		326.8
320		268.3
325		234.7
330		218.2
335		196.0
340		181.0
345		182.1
350		215.0
355		324.2
360		452.0

sents the number of P_n travel time picks in a 20° azimuthal interval centered at the azimuth. The average is 241.1, roughly equivalent to 70 picks in 20° intervals. None of the average velocity residuals exceeds 1% (Figure 5). The average velocity residuals at azimuth 80° - 100° are about 0.9%. However, the denominator values for their 20° interval are less than half of the average (Table 1). The error bars are mostly larger than 2%. Thus the azimuthal anisotropy in P_n velocity, if any, is not likely to be greater than 1% for the Basin and Range province.

ERROR ANALYSIS AND RESOLUTION OF THE P_n VELOCITY IMAGE

In this section, we quantitatively assess the quality of the two-dimensional P_n velocity image obtained in this study. We also present the P_n velocity images, (1) without correcting for a mantle velocity gradient and (2) assuming a homogeneous crust and mantle.

In tomography the spatial resolution at a given grid can be approximated by the point spreading function (psf) cal-

culated for the grid [e.g., Humphreys and Clayton, 1988; Xie and Mitchell, 1990]. We calculated the psf for six grids, five close to the boundaries, one in the center of the region (Figure 6a). We put three grids of the psf on one plot, since they do not overlap each other. The spatial resolution is generally less than 3° , and less than 2° at locations where the ray coverage is better. However, the grid beneath Sierra Nevada (the lower dark one of Figure 6a) spreads about 5° . This is caused by parallel rays passing through most of the area. However, the point spreading function gives only the resolution that can be achieved from the given ray path coverage.

Figure 7 gives the velocity image without correcting for mantle velocity gradient, that is, $\gamma' = 0.0$. The average velocity is $7.73 \pm 0.16 \text{ km s}^{-1}$. The main pattern of the velocity distribution of Figure 7 is about same as that of Figure 4. However, the slower P_n velocity regions in the south are smaller and not connected to each other in Figure 7, as compared with that in Figure 4. The small difference in Figures 4 and 7 is due to small positive mantle velocity gradient, $2.0 \times 10^{-3} \text{ s}^{-1}$.

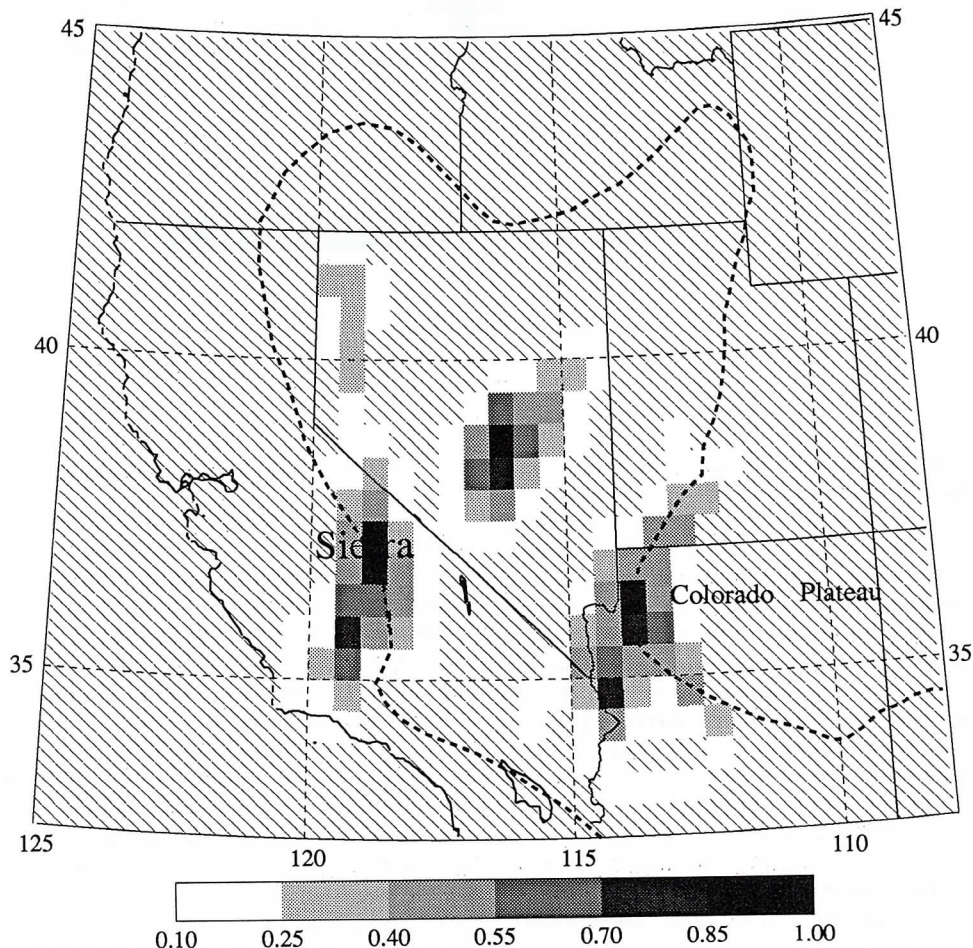


Fig. 6. Point spread functions (psf) for six grids, five close to the boundaries, one in the center of the region. Without losing any information, we put three grids in one plot, since they do not overlap. (a) The point spread function of the middle grid 2° , left grid 5° , and right grid 3° ; and (b) The point spread function of the left grid spreads 2° , lower grid 2° , and right grid 2.5° . Heavy dashed lines depict the boundaries of the Basin and Range province. The diagonally ruled area indicates an area with insufficient resolution, or with the amplitude less than 0.1.

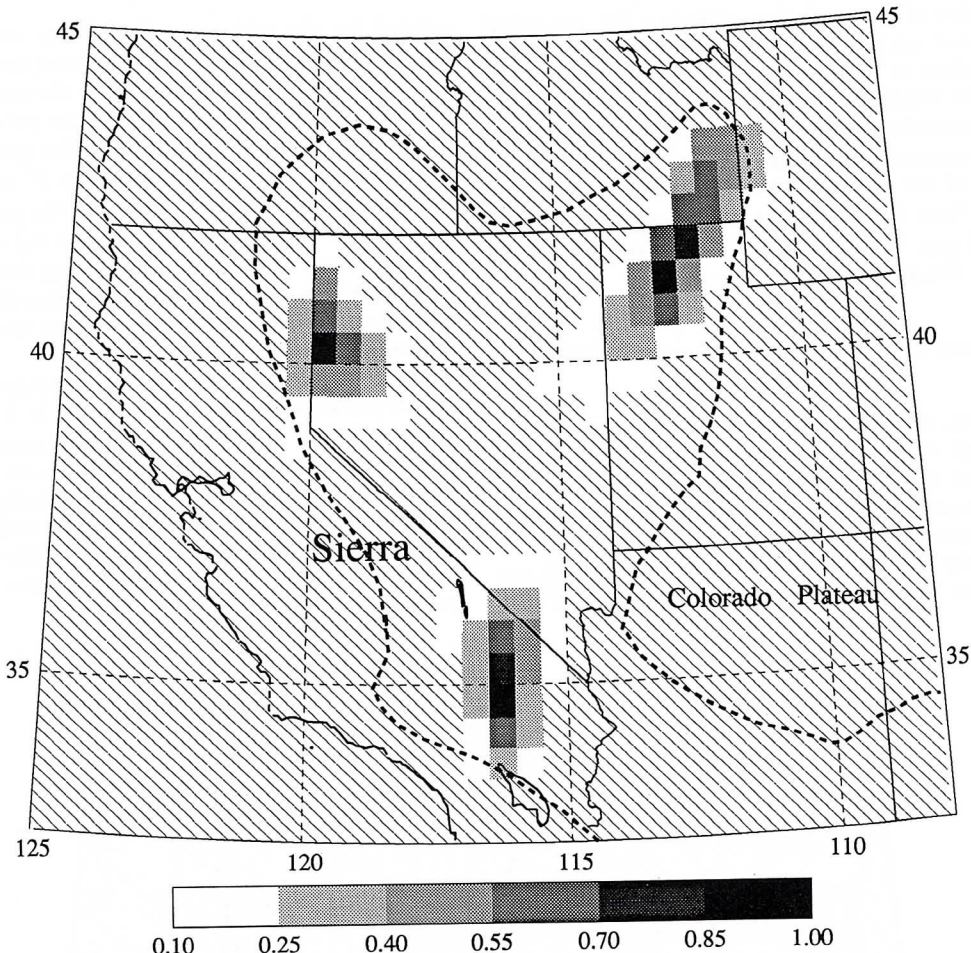


Fig. 6. (continued)

As has been discussed before, we used the crustal and upper mantle velocity models of seismic sounding studies to estimate α' and β' from (2). In this section we show the results from the assumption of a homogeneous uppermost mantle velocity model, which is an average model of the Basin and Range province [Braile et al., 1989], with a compressional velocity of 6.25 km s^{-1} for the crust and 7.8 km s^{-1} for the mantle, and with a thickness of 35 km , for the whole Basin and Range province. The α' and β' values estimated also from (2). The velocity image is given in Figure 8. The average P_n velocity of $7.77 \pm 0.16 \text{ km s}^{-1}$ in Figure 8 is higher than that of 7.72 km s^{-1} in Figure 4. The main features of the velocity distribution are similar except for the southern end, at which the P_n velocities are much exaggerated. The slow regions are reduced beneath the Sierra Nevada and southern Nevada (Figures 4 and 8). The fast regions are expanded; for example, see northern portion of the study area. The southern end of the study area, close to the Gulf of California, P_n velocities become fast (Figure 8), which is very similar to the results of Hearn et al. [1991]. The actual crustal thickness in the region of the south end is about 25 km [Braile et al., 1989], 10 km thinner than what was used. Thus α' or β' is about 1 s greater than α and β , the travel time is smaller for any ray ending within this region.

ERROR ANALYSIS OF AZIMUTHAL ANISOTROPY

The azimuthal velocity residuals plotted in Figure 9 are calculated from the P_n velocity image given in Figure 7, without correcting the mantle velocity gradient. The averaged values are almost identical to that derived from a model with a positive velocity gradient mantle. This implies that the assumption of a homogeneous mantle does not affect the velocity residual dependence on azimuth. However, the two-station method of Beghoul and Barazangi [1990] tends to enlarge the contribution of the mantle velocity gradient to the velocity residuals. For example, the P_n velocities from the two-station method are 7.82 km s^{-1} for distance of 500 km (two-stations at 1000 and 1500 km) and 7.73 km s^{-1} for distance of 300 km (two-stations at 200 and 500 km) instead of the real velocity of 7.72 (200 km) and 7.73 (500 km), using $v_0 = 7.72 \text{ km s}^{-1}$ and $c = 2.56 \times 10^{-4} \text{ km}^{-1}$ obtained previously. The correction of the average mantle velocity gradient should not affect the azimuthal anisotropy, since the correction is the same in every direction.

Assuming a homogeneous model for both crust and mantle, we obtained the velocity image given in Figure 8, the azimuthal velocity residuals of which are given in Figure 10. The similarity of Figure 5 to Figure 10 infers that the initial crustal models do not affect the azimuthal depen-

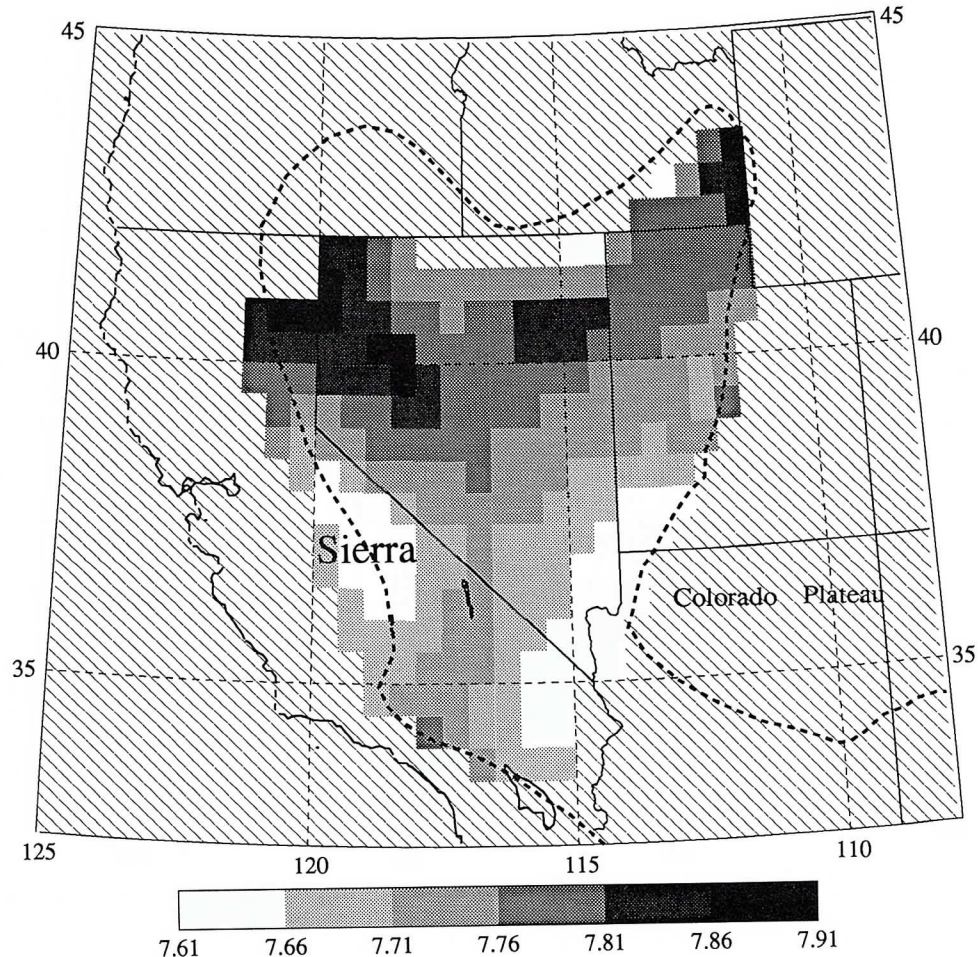


Fig. 7. P_n velocity image for the Basin and Range province without correcting for mantle velocity gradient, that is, assuming $\gamma' = 0.0$ s. The diagonally ruled area indicates an area with insufficient resolution.

dence of the velocity residuals. Note that the contributions of the lateral variation of the P_n velocities, the mislocation of the events, and lateral variation of the crustal structure to the azimuthal P_n velocity residuals were taken out in the course of inversion and allocation procedure.

We use the refined P_n travel time data set, which is not yet put through the last inversion to get the tomographic image in Figure 8. This means that the lateral variations in the P_n velocities is put back to the travel times, and the α and β values are refined. The average velocity of 7.77 ± 0.16 km s^{-1} was given above for this data set (Figure 8). We use this values as the velocity for the upper mantle beneath the whole studied area (homogeneous). The azimuthal velocity residuals are given in Figure 11. The fluctuation of the averaged velocity residuals is larger than the residuals shown in Figure 5.

Figure 12 gives the azimuthal velocity residuals for the raw data with correcting a homogeneous crust and upper mantle. The average velocity is 7.77 ± 0.20 km s^{-1} . The standard error is larger than that in Figure 11. The pattern of Figure 12 is roughly the same as that of Figure 11. This figure suggests that as long as the ray paths are dense, there is no evidence for azimuthal anisotropy in the Basin and Range province, regardless of the assumptions made in the crustal and mantle velocity structures.

DISCUSSION AND CONCLUSIONS

P_n Velocity Image

The inversion method and procedure used in this study to get the P_n velocity image differ from those in previous P_n tomography studies [e.g., Hearn et al., 1991]. We used the following two steps prior to the back projection inversion:

1. We estimated the vertical travel times for the sources and receivers, with a priori knowledge on the lateral variation of crustal structure. These delay times were then subtracted from the P_n travel times to obtain the apparent P_n velocity.

2. We estimated the average mantle velocity gradient, which was used to correct the apparent P_n velocities to get P velocities along the uppermost mantle.

The numerical experiment and theoretical development, which make these two corrections possible, are given in this study.

The average P_n velocity from the inversion is 7.72 ± 0.16 km s^{-1} . The average mantle velocity gradient obtained in this study is 2.0×10^{-3} s $^{-1}$, including the contribution of the Earth's sphericity, 1.2×10^{-3} s $^{-1}$. Two distinct low P_n velocity regions beneath the Sierra Nevada mountains and southern Nevada seem to be connected and form one

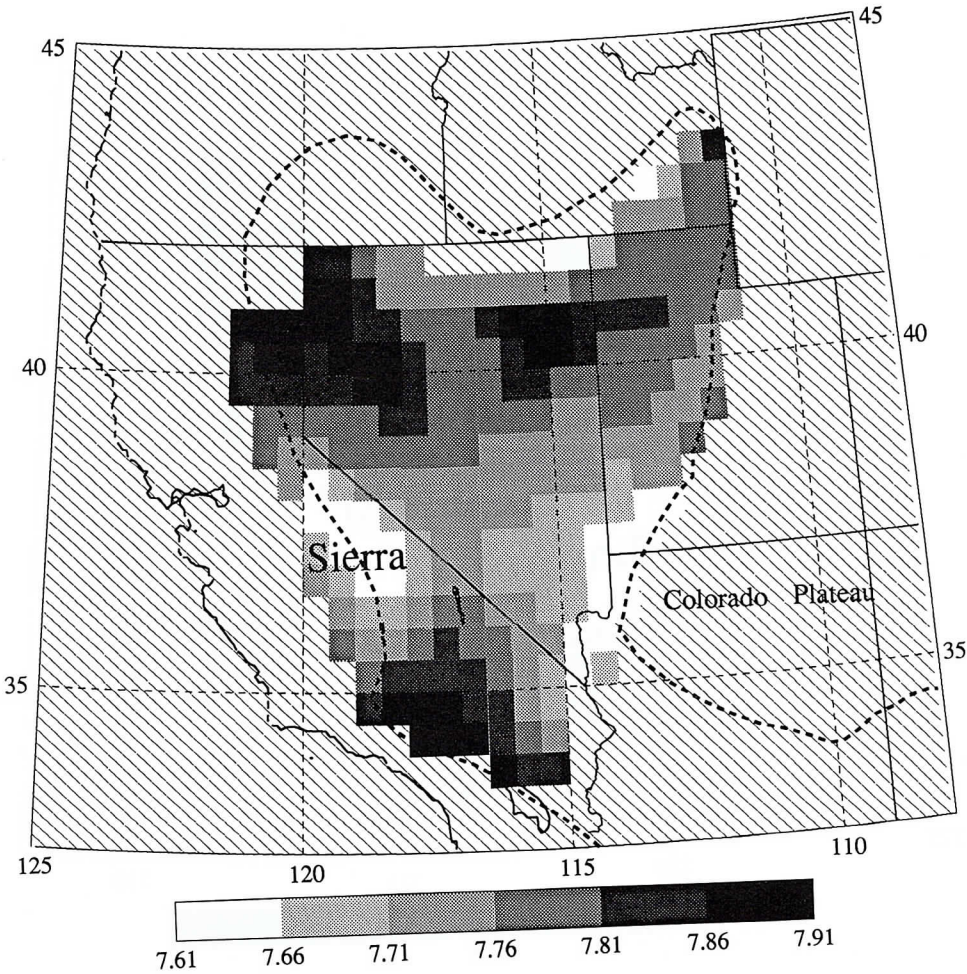


Fig. 8. P_n velocity image for the Basin and Range province assuming a homogeneous crust and mantle.

large low-velocity region in the southern Basin and Range province. The P_n velocity is less than 7.8 km s^{-1} in the south; and it is greater than the 7.8 km s^{-1} in the north. These slow and fast regions form two big E-W strips (Figure 4). The P_n velocity pattern of low-south and fast-north regions, in an almost E-W direction, could be due to upwelling beneath the Sierra Nevada and crustal extension in the southern Nevada, as discussed above. Also, it may suggest that a small convection current occurred here in the region, upwelling in the south and downwelling in the north beneath the Basin and Range province, if the velocity differences are caused by the temperature.

The P_n velocity image is not affected much by the mantle velocity gradient. However, the three-dimensional crustal structure is crucial to the P_n velocity image. The lower- or faster-velocity pattern is largely the result of the too short or too long estimates of the source and receiver delay times. The resolution of the velocity image is generally within 3° , within 2° for the grids with denser ray coverage and within 5° for poorer ray coverage grids.

Azimuthal Anisotropy of P_n Velocities

The method used in this study to infer the P_n velocity anisotropy also differs from previous studies [e.g., Vetter and Minster, 1981], in two following ways: 1. most impor-

tant of all, we took away the lateral variation in P_n velocities from the possible azimuthal dependence of the velocity residuals by using tomographic inversion; and 2. we relocated the sources and refined of the local crustal structures beneath the sources and receivers.

P_n azimuthal anisotropy for this region, if any, is not likely to be greater than 1% from velocity residuals calculated from various models. However, previous P_n studies suggested more than 3% anisotropy [Vetter and Minster, 1981; Beghou and Barazangi, 1990]. The obvious reason for this discrepancy is the heterogeneity and the much larger volume of the present data set. An azimuthal dependence might show up if the stations were located within some limited region as the case considered by Vetter and Minster [1981]. For example, all stations are located in the center of the region with earthquakes around them (Figure 8). The seismic anisotropy in this method is merely the lateral variation. The two-station method, which was used by Beghou and Barazangi [1990] to estimate P_n velocities for this region, does not account for the mantle velocity gradient. Mantle velocity gradient and lateral variations of P_n velocities are responsible for the anisotropy in this case.

For the azimuthal velocity residuals the effects of the mantle velocity gradient and the initial crustal models are small. The lateral variation of the P_n velocities and refinements of the vertical travel times of the sources and

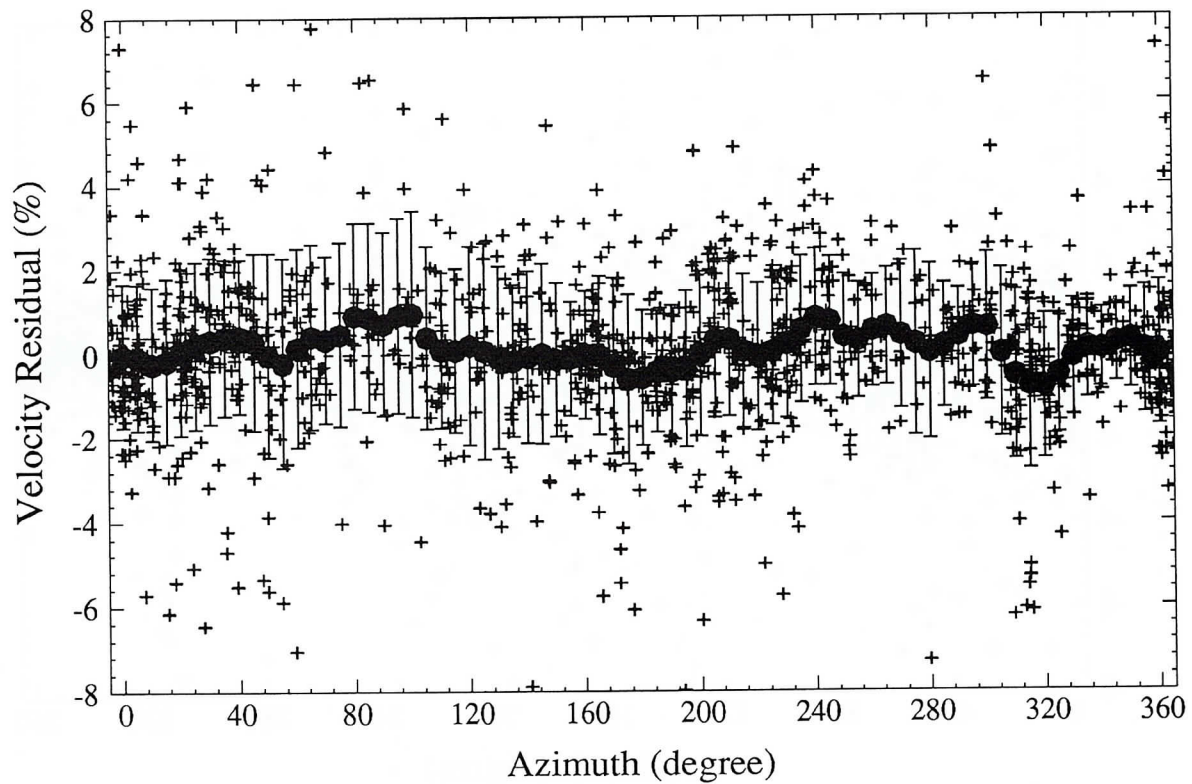


Fig. 9. Velocity residuals, averaged velocity residuals after correcting the velocity distribution of Figure 7, versus the azimuths of the paths.

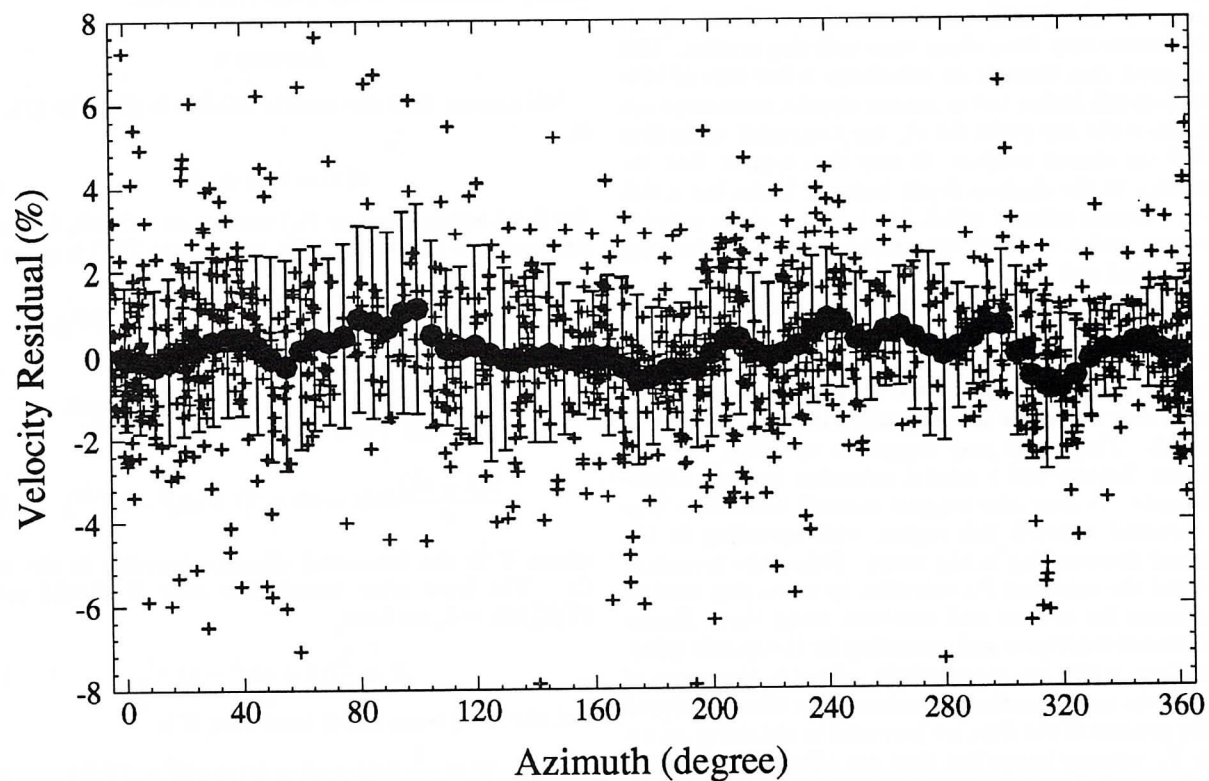


Fig. 10. Velocity residuals, averaged velocity residuals after correcting the velocity distribution of Figure 8, versus the azimuths of the paths.

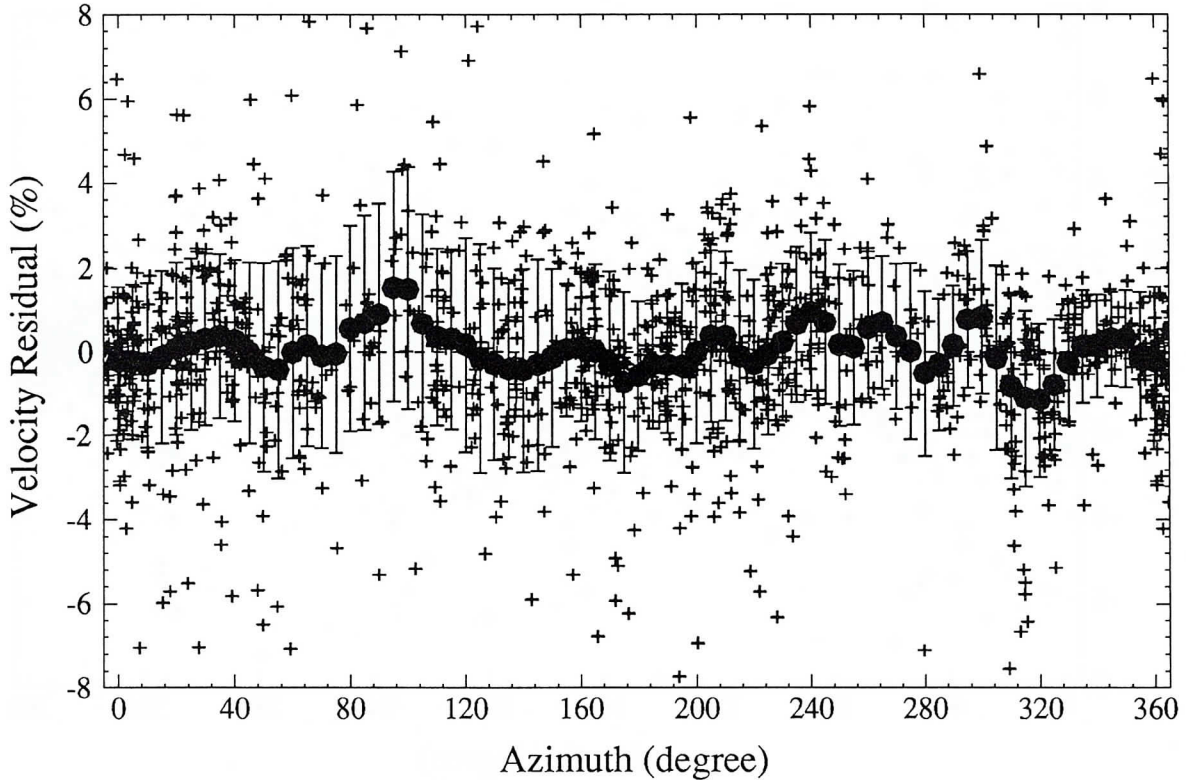


Fig. 11. Velocity residuals, averaged velocity residuals before correcting the velocity distribution of Figure 8, versus the azimuths of the paths.

receivers are substantial; they affect both the amplitude and general pattern.

Savage et al. [1990] found favorable evidence of azimuthal anisotropy from shear wave splitting studies. This may suggest that there is no anisotropy a few tens of kilometers beneath Moho, but at greater depths, anisotropy appears, since the ray paths for P_n are horizontal while that of SKS are almost vertical. It may also suggest that the mineralogy at the shallow depth beneath Moho has a rich content of some mineral which has a strong shear velocity anisotropy and a weak compressional velocity anisotropy, such as spinel and rutile.

In conclusion, we applied the tomographic inversion method to 1226 P_n travel times from ISC catalogs to study the P_n velocity distribution and anisotropy beneath the Basin and Range province. We obtained a velocity image with slow velocities in the south and fast velocities in the north. The image may suggest an upwelling beneath the Sierra Nevada and a crustal extension beneath southern Nevada. It may also suggest a small convection current occurred beneath this region, with upwelling in the south and downwelling in the north. Before the inversion, we refined the apparent P_n velocities by correcting vertical travel times for sources and receivers using three dimensional crustal structures and correcting for the mantle velocity gradient, which are progressively refined in the course of the inversion and allocation procedure. The aforementioned refining process of the data set is crucial in obtaining an accurate P_n velocity image but does not affect the azimuthal dependence of the velocity residuals, although the amplitude of these is increased. Azimuthal anisotropy in the uppermost mantle beneath the Basin and Range province

is very small, less than 1%, if present at all, in spite of the strong orientation of the local stress fields.

APPENDIX

We assume that the mantle velocity is given by (3), that is,

$$v(z) = v_0(1 + cz). \quad (\text{A1})$$

For head waves (such as P_n) turning at a depth, h , the ray parameter is $1/v(h)$, and the travel time $T(h)$ is given by

$$\begin{aligned} T(h) &= \frac{X}{v(h)} + 2 \int_0^h \left(\frac{1}{v(z)^2} - \frac{1}{v(h)^2} \right)^{1/2} dz \\ &= \frac{1}{v_0(1 + ch)} [X - \frac{2}{c} ((1 + ch)^2 - 1)^{1/2} \\ &\quad + \frac{2(1 + ch)}{c} \ln(1 + ch + ((1 + ch)^2 - 1)^{1/2})], \end{aligned} \quad (\text{A2})$$

where X is the horizontal distance traveled in the mantle. The head wave travel time over X should satisfy $dT(h)/dh = 0$, we have

$$X = \frac{2}{c} ((1 + ch)^2 - 1)^{1/2}, \quad (\text{A3})$$

and the head wave travel time over X is

$$T = \frac{2}{v_0 c} \ln(1 + ch + ((1 + ch)^2 - 1)^{1/2}). \quad (\text{A4})$$

From definition, The observed head wave velocity is $v_{obs} = X/T$. From (A3) and (A4) we have

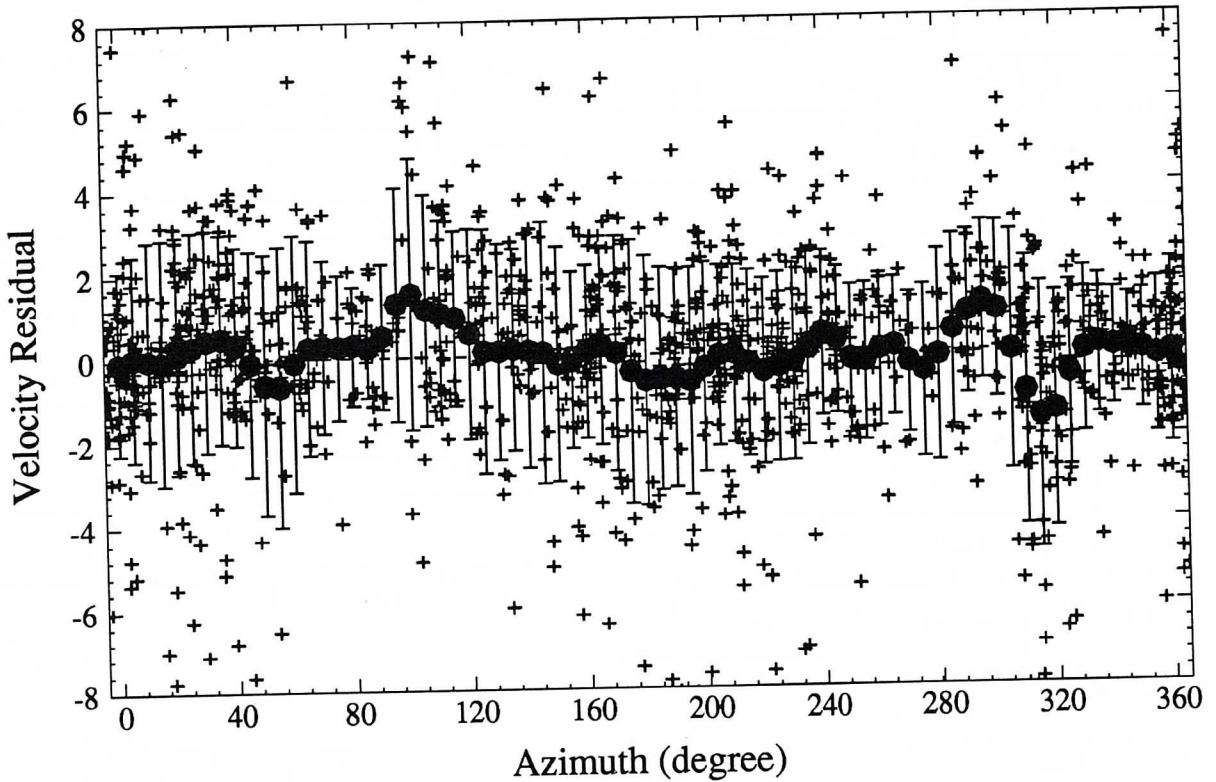


Fig. 12. Velocity residuals, averaged velocity residuals versus the azimuths of the paths. The data used in this figure are the raw data after correcting the vertical travel times for the sources and receivers assuming a homogeneous crust and mantle, is the same as that which produced the velocity image in Figure 8 and residuals in Figure 10, before the inversion and allocation procedure have begun.

$$v_{obs} \approx v_0 \frac{\sqrt{2ch}(1+ch/4)}{\ln(1+ch+\sqrt{2ch}(1+ch/4))}$$

$$\approx v_0 \frac{\sqrt{2ch}(1+ch/4)}{\sqrt{2ch}(1-ch/12)} \approx v_0(1+\frac{ch}{3}), \quad (A5)$$

if $ch \ll 1$. For $ch \ll 1$, X can be approximated by

$$X \approx \sqrt{8h/c}, \quad h \approx cX^2/8. \quad (A6)$$

Substituting (A6) into (A5), we have (4) in the text.

$$v_{obs} \approx v_0(1+c^2X^2/24).$$

If $X > X_m = ((1+cH_m)^2 - 1)^{1/2}/c$, at which the ray bottoms the depth of H_m , below which (A1) does not hold, (A4) should be written as

$$T = \frac{X - X_m}{v_0(1+cH_m)} + \frac{2}{v_0c} \ln(1+cH_m + ((1+cH_m)^2 - 1)^{1/2})$$

$$\approx \frac{X - X_m}{v_0(1+cH_m)} + \frac{X_m}{v_0(1+\frac{1}{3}cH_m)}$$

$$\approx \frac{X + \frac{2}{3}X_m cH_m}{v_0(1+cH_m)}.$$

From the definition of $v_{obs} = X/T$, we have

$$v_{obs} \approx \frac{1 + \frac{2X_m}{3X} cH_m}{v_0(1+cH_m)} \approx v_0 + v_0 cH_m \left(1 - \frac{2X_m}{3X}\right),$$

which is (5) in the text.

Acknowledgments. I would like to thank Don L. Anderson for his suggestions and Robert W. Clayton for showing me how to read his 1964-1986 ISC catalogs. I would also like to thank Don L. Anderson, James Ni, and Bradley Woods for their review of the manuscript, and Ilya Tsvankin and John Scales for their reviews and comments. This research was supported by the Air Force Office of Scientific Research under grant F49620-92-J-0470. Contribution 5216, Division of Geological and Planetary Sciences, California Institute of Technology, Pasadena, California.

REFERENCES

- Anderson, D. L., *Theory of the Earth*, Blackwell Scientific, Boston, Mass. 1989.
- Bamford, D., M. Jentsch, and C. Prodehl, P_n anisotropy studies in northern Britain and the eastern and western United States, *Geophys. J. R. astron. Soc.*, 57, 397-429, 1979.
- Beghoul, N., and M. Barazangi, Azimuthal anisotropy of velocity in the mantle lid beneath the basin and range province, *Nature*, 348, 536-538, 1990.
- Biassi, G. P., and E. D. Humphreys, P-wave image of the upper mantle structure of central California and southern Nevada, *Geophys. Res. Lett.*, 19, 1161-1164, 1992.
- Braile, L. W., W. J. Hinze, R. R. B. von Frese, and G. R. Keller, Seismic properties of the crust and uppermost mantle of the conterminous United States and adjacent Canada, in *Geophysical framework of the continental United States*, edited by L. C. Pakiser and W. D. Mooney, Geol. Soc. Am. Mem. 172, 655-679, 1989.

- Burdick, L. J., and D. V. Helmberger, The upper mantle P velocity structure of the Western United States, *J. Geophys. Res.*, **83**, 1699-1712, 1978.
- Duffy, T. S., and D. L. Anderson, Seismic velocities in mantle minerals and the mineralogy of the upper mantle, *J. Geophys. Res.*, **94**, 1895-1912, 1989.
- Hearn, T., N. Beghoul, and M. Barazangi, Tomography of the western United States from regional arrival times, *Geophys. J. Res.*, **96**, 16,369-16,381, 1991.
- Helmberger, D. V., Numerical seismograms of long-period body waves from seventeen to forty degrees, *Bull. Seismol. Soc. Am.*, **63**, 633-646, 1973.
- Hess, H., Seismic anisotropy of the uppermost mantle under oceans, *Nature*, **203**, 629-631, 1964.
- Humphreys, E., and R. W. Clayton, Adaptation of back projection tomography to seismic travel time problems, *J. Geophys. Res.*, **93**, 1073-1086, 1988.
- Jones, C. H., H. Kanamori, and S. W. Roecker, Missing roots and mantle "drips": Regional P_n and teleseismic arrival times in the southern Sierra Nevada and vicinity, California, *J. Geophys. Res.*, in press, 1993.
- Park, J., and Y. Yu, Anisotropy and coupled free oscillations: Simplified models and surface wave observations, *Geophys. J. Int.*, **110**, 401-420, 1992.
- Rait, R. W., G. G. Shor, T. J. G. Francis, and H. H. Kirk, Mantle anisotropy in the Pacific Ocean, *Tectonophysics*, **12**, 1971.
- Savage, M. K., P. G. Silver, and R. P. Mayer, Observations of teleseismic shear-wave splitting in the basin and range from portable and permanent stations, *Geophys. Res. Lett.*, **17**, 21-24, 1990.
- Silver, P. G., and W. W. Chan, Implications for continental structure and evolution from seismic anisotropy, *Nature*, **335**, 34-39, 1988.
- Silver, P. G., and W. W. Chan, Shear-wave splitting and subcontinental mantle deformation, *J. Geophys. Res.*, **96**, 16,429-16,454, 1991.
- Suetsugu, D., and I. Nakanishi, Tomographic inversion and resolution for Rayleigh wave phase velocities in the Pacific Ocean, *J. Phys. Earth*, **33**, 345-368, 1985.
- Tanimoto, T., and D. L. Anderson, Lateral heterogeneity and anisotropy of the upper mantle 100-200s, *J. Geophys. Res.*, **90**, 1842-1858, 1985.
- Vetter, U., and J. B. Minster, P_n velocity anisotropy in southern California, *Bull. Seismol. Soc. Am.*, **71**, 1511-1530, 1981.
- Vidale, J. E., D. V. Helmberger, and R. W. Clayton, Finite-difference seismograms for SH waves, *Bull. Seismol. Soc. Am.*, **75**, 1765-1782, 1985.
- Xie, J., Shear wave splitting near Guam, *Phys. Earth Planet. Int.*, **72**, 211-219, 1992.
- Xie, J., and B. J. Mitchell, A back-projection method for imaging large-scale lateral variations of Lg coda Q within application to continental Africa, *Geophys. J. Int.*, **100**, 161-181, 1990.
- Yu, Y., and J. Park, Upper mantle anisotropy and coupled-mode long-period surface waves, *Geophys. J. Int.*, in press, 1993.

L.-S. Zhao, Institute for Geophysics, University of Texas at Austin,
8701 N. MoPac Blvd. Austin, TX 78759-8345.

(Received December 21, 1992;
revised August 10, 1993;
accepted September 13, 1993.)